2. H. London, *Z. Phys. Chem.* **16**, 302 (1958).
3. P. Pavone and S. Baroni, *Solid State Commun.* **90**, 295 (1994).
4. A. Debernardi and M. Cardona, *Phys. Rev. B* **54**, 11305 (1996).
5. N. Garro *et al.*, *ibid.*, p. 4732.
6. J. C. Noya, C. P. Herrero, R. Ramírez, *ibid.* **56**, 237 (1997).
7. H. Holloway, K. C. Hass, M. A. Tamor, T. R. Anthony, W. F. Banholzer, *ibid.* **44**, 7123 (1991).
8. C. Buschert, A. E. Merlini, S. Pace, S. Rodriguez, M. H. Grimsditch, *ibid.* **38**, 5219 (1988).
9. C. Parks, A. K. Ramdas, S. Rodriguez, K. M. Itoh, E. E. Haller, *ibid.* **49**, 14244 (1994).
10. S. Zollner, M. Cardona, S. Gopalan, *ibid.* **45**, 3376 (1992).
11. The epitaxial film of the highly enriched ^{76}Ge isotope (average mass 75.63) was grown on an intrinsic Ge(111) substrate in an ultrahigh vacuum system (base pressure 10^{-11} mbar) by molecular beam epitaxy at a substrate temperature of 720 K, well below the threshold for bulk interdiffusion [H. D. Fuchs *et al.*, *Phys. Rev. B* **51**, 16817 (1995)]. Before and after the growth of the sample, reference films were grown and their thickness was measured with a step stylus to calibrate the growth rate, which was 1.0 ± 0.07 nm/min, as also found by a quartz microbalance. The thickness of the film is determined by the duration of growth.
12. J. Honstra and W. J. Bartels, *J. Cryst. Growth* **44**, 513 (1978).
13. M. v. Laue, *Röntgenstrahlinterferenzen* (Akademische Verlagsgesellschaft, Frankfurt/Main, 1960).
14. B. W. Batterman, *Phys. Rev. A* **133**, 759 (1964).
15. J. Zegenhagen, *Surf. Sci. Rep.* **18**, 199 (1993).
16. For the escape depth of the Ge-L photoelectrons, we used μ^{-1} = 59 nm calculated by Kovalchuk *et al.* [M. V. Kovalchuk, D. Liljequist, V. G. Kohn, *Sov. Phys. Solid State* **28**, 1918 (1986)] by Monte Carlo simulation.
17. A. Krolzig, G. Materlik, J. Zegenhagen, *Nucl. Instrum. Methods* **208**, 613 (1983).
18. We used an algorithm proposed by Kohn [V. G. Kohn and M. V. Kovalchuk, *Phys. Stat. Sol.* **A64**, 359 (1981)] based on the Takagi-Taupin equations using recurrent relations for the amplitude ratio E_h/E_0 of reflected and incident wave and the intensity of the refracted wave $I_0 = |E_0|^2$ to calculate the total field distribution in the semi-infinite sample and the epitaxial overlayer with a different lattice constant. By fitting the curve for the lowest temperature (T = 54 K), the static Debye-Waller factor of the film was determined to be e^{-W} = 0.76, which was used with the thermal Debye-Waller factors for germanium [B. W. Batterman and D. R. Chipman, *Phys. Rev.* **127**, 690 (1962)] for fitting all experimental data.
19. We are grateful to V. Kohn for the computer code for the analysis based on the Takagi-Taupin equation, to K. Eberl and E. Gmelin for valuable discussions, and to W. Stiepany, P.-Y. Lowys, G. Schneider, T. Chaperon, M. Siemers, and A. Riccardi for technical assistance.

7 July 1998; accepted 24 September 1998

Spontaneous Emission Spectrum in Double Quantum Dot Devices

Toshimasa Fujisawa, Tjerk H. Oosterkamp, Wilfred G. van der Wiel, Benno W. Broer, Ramón Aguado, Seigo Tarucha, Leo P. Kouwenhoven*

A double quantum dot device is a tunable two-level system for electronic energy states. A dc electron current was used to directly measure the rates for elastic and inelastic transitions between the two levels. For inelastic transitions, energy is exchanged with bosonic degrees of freedom in the environment. The inelastic transition rates are well described by the Einstein coefficients, relating absorption with stimulated and spontaneous emission. The most effectively coupled bosons in the specific environment of the semiconductor device used here were acoustic phonons. The experiments demonstrate the importance of vacuum fluctuations in the environment for quantum dot devices and potential design constraints for their use for preparing long-lived quantum states.

Electronic quantum devices allow the quantum mechanical properties of electrons confined to small regions in a solid to be explored. Existing devices include semiconductor resonant tunneling diodes (*1*) (based on quantum mechanical confinement), superconducting Josephson junction circuits (*2*) (based on macroscopic phase coherence), metallic single-electron transistors (*3*) (based on quantization of charge), and molecular electronic devices (*4*). The principle of operation in circuits of these devices is based on controlling energy states, for instance, by means of an external (gate) voltage. Thermal energy is always a source for unwanted transitions and errors. Even at zero temperature, however, vacuum fluctuations in the environment can give rise to transitions between states of nonequal energy by spontaneous emission of an energy quantum. Such inelastic transitions cause errors in many proposed schemes for quantum circuits. Here we studied inelastic transitions in a fully controllable, two-level quantum system realized in a double quantum dot device. We can relate the transition rates involving emission to absorption rates by the Einstein coefficients over the full energy and temperature range we studied. At the lowest temperature (23 mK), we directly measured the energy-dependent rate for spontaneous emission and determined that, in our specific semiconductor device, this energy is emitted into the environment formed by acoustic phonons.

Our double quantum dot (Fig. 1A) is fabricated in the two-dimensional electron gas (2DEG) of an AlGaAs-GaAs semiconductor heterostructure (*5*). The source and drain are large 2DEG regions that serve as leads for contacting current and voltage wires. The two dots, L and R, are separated from each other and from the leads by potential barriers induced by negative voltages applied to the three metallic gates. Tunneling between the different regions is sufficiently strong to detect current but weak enough that the number of electrons in each dot is a well-defined integer. The energy states in such fully confined regions are discrete, 0D states, resembling discrete atomic states (*6, 7*). The discrete energies include contributions from single-electron charging energies (arising from Coulomb interactions) and from quantum-mechanical confinement. The lowest energy state for one additional electron in the L dot is labeled in Fig. 1, B to D, as E_L, and similarly E_R for the R dot. Figure 1C illustrates the resonance condition, $E_L = E_R$, in which case an electron can tunnel elastically from an occupied state in the source via E_L and E_R to an empty state in the drain. Such tunneling sequences of single electrons are regulated by the Coulomb charging energies (*3, 7*). When the two states are not aligned, $E_L \neq E_R$, only inelastic transitions are allowed for which some energy needs to be exchanged with the environment. A measured off-resonance current, therefore, directly provides information about the coupling between electrons on the dots to degrees of freedom in the environment. The inelastic rates can be analyzed with well-developed methods in quantum optics (*8, 9*).

A typical current spectrum versus $\varepsilon \equiv E_L - E_R$ at our lowest lattice temperature T = 23 mK (*10*) is shown in Fig. 1E. The gate voltages V_{GR} and V_{GL} are swept simultaneously such that the respective energies are like those illustrated in Fig. 1, B to D; that is, ε = 0 occurs in the middle between the Fermi energies of source and drain, μ_S and μ_D, and $|\varepsilon| = eV_{SD}$ (its maximum) corresponds to having the states E_L and E_R aligned to one of the Fermi energies. To analyze the large asymmetry, we decomposed the total current $I_{tot}(\varepsilon) = I_{el}(\varepsilon) + I_{inel}(\varepsilon > 0)$ into a symmetric part $I_{el}(\varepsilon) = I_{el}(-\varepsilon)$ (dashed curve) and the remaining asymmetric part $I_{inel}(\varepsilon > 0)$ (dotted-dashed curve). At T = 0, $I_{el}(\varepsilon)$ is due

T. Fujisawa, Department of Applied Physics and DIMES, Delft University of Technology, 2600 GA Delft, Netherlands, and NTT Basic Research Laboratories, 3-1, Morinosato-Wakamiya, Atsugi, Kanagawa, 243-0198, Japan. T. H. Oosterkamp, W. G. van der Wiel, B. W. Broer, R. Aguado, L. P. Kouwenhoven, Department of Applied Physics and DIMES, Delft University of Technology, 2600 GA Delft, Netherlands. S. Tarucha, NTT Basic Research Laboratories, 3-1, Morinosato-Wakamiya, Atsugi, Kanagawa, 243-0198, Japan, and Department of Physics, University of Tokyo, 7-3-1 Hongo, Bunkyo-ku, Tokyo 113-0033, Japan.

*To whom correspondence should be addressed. E-mail: leo@qt.tn.tudelft.nl

to elastic tunneling and has a Lorentzian line shape $I_{el}(\varepsilon) = I_{el,max}\omega^2/(\omega^2 + \varepsilon^2)$ (*11*). The full width at half maximum, 2ω, can be tuned by the central gate voltage V_{GC} roughly from 4 to 20 μeV. From measurements of $I_{el}(\varepsilon)$ at positive and negative V_{SD}, it is possible to extract values for the tunnel couplings Γ_L, Γ_R, and T_c (*11, 12*).

The remaining current, $I_{inel}(\varepsilon > 0)$, which is nonzero only for $\varepsilon > 0$, is due to inelastic tunneling. In Fig. 1E, I_{inel} is nonzero over an energy range of ~100 μeV, despite the thermal energy kT (23 mK) = 2 μeV being much smaller (k is Boltzmann's constant). (The irregular fine structure is discussed below.) In general, we found that I_{inel} vanishes when one of the levels, E_L or E_R, crosses one of the two Fermi energies. In the specific case of Fig. 1E, E_L and E_R cross the Fermi energies simultaneously, implying that I_{inel} is cut off at $\varepsilon = eV_{SD}$. Below this cutoff, the value of I_{inel} was not influenced by the value of V_{SD} (*13*). For $T = 0$, we can write the condition for a nonzero inelastic current as $\mu_S > E_L > E_R > \mu_D = \mu_S - eV_{SD}$. The amount of inelastic current depends on the transition rates as $I_{inel}(\varepsilon) = e[\Gamma_L^{-1} + \Gamma_i^{-1}(\varepsilon) + \Gamma_R^{-1}]^{-1}$. When the inelastic rate $\Gamma_i(\varepsilon)$ from E_L to E_R is much smaller than the rates through the outer barriers, then $I_{inel}(\varepsilon) = e\Gamma_i(\varepsilon)$.

The effect of a nonzero temperature on the current is shown in Fig. 2A. A higher temperature T enhances I_{tot} on both the emission ($\varepsilon > 0$) and the absorption ($\varepsilon < 0$) side. The absorption spectrum shows an exponential temperature dependence, $e^{\varepsilon/kT}$ (dashed lines), for absolute energies larger than the elastic current measured at 23 mK, that is $|\varepsilon| > w$.

To analyze the temperature dependence, we assumed boson statistics for the degrees of freedom in the environment. The average occupation number $\langle n\rangle$ of environmental modes at energy ε is given by the Bose-Einstein distribution function: $\langle n\rangle = 1/(e^{\varepsilon/kT} - 1)$. The rates for absorption, W_a, and emission, W_e, can be expressed very generally by $W_a = B_a\rho$ and $W_e = A + B_e\rho$, where the Einstein coefficients stand for spontaneous emission (A) and stimulated emission (B_e) and absorption (B_a), and ρ is the energy density (*8*). From the Einstein relations, $B_a = B_e = A\langle n\rangle/\rho$ (*8*), we obtain

$$\Gamma_i(\varepsilon < 0) = W_a(\varepsilon) = \langle n\rangle A(-\varepsilon) \quad (1)$$

$$\Gamma_i(\varepsilon > 0) = W_e(\varepsilon) = (\langle n\rangle + 1)A(\varepsilon)$$

To test whether the inelastic current follows emission and absorption statistics, we calculated the full current spectrum from Eq. 1. First, we obtained the spontaneous emission rate from $A(\varepsilon) = I_{inel}(\varepsilon > 0, T = 23\ \text{mK})/e$. The trace at 23 mK is effectively at zero temperature for $\varepsilon \gg 2$ μeV because then $\langle n\rangle \ll 1$. The emission current at higher temperatures follows from $I_{inel}(\varepsilon > 0, T) = e(\langle n\rangle + 1)A(\varepsilon)$, whereas the absorption current follows from $I_{inel}(\varepsilon < 0, T) = e\langle n\rangle A(-\varepsilon)$. The reconstructed current spectrum is shown in Fig. 2B. The central part of the curves ($|\varepsilon| < 10$ μeV) is kept blank because Eq. 1 does not include the T dependence of I_{el}. The calculated current reproduces the measured current well up to 200 mK. Even the small steplike feature seen at $\varepsilon \sim 30$ μeV is reflected by a shoulderlike feature at $\varepsilon \sim -30$ μeV in the measured and in the calculated absorption spectra (indicated by arrows). For $T > 200$ mK, the measured current significantly exceeds the calculated current, which is probably due to thermally excited electrons. (Equation 1 only describes the T dependence of the environment. The thermal excitations in the electron leads are not included.) Further confirmation of the applicability of the Einstein relations to our quantum dot system follows from the prediction $[I_{inel}(\varepsilon > 0) - I_{inel}(\varepsilon < 0)]/eA(|\varepsilon|) = [W_e - W_a]/A = 1$, which is valid independent of T. A plot of the normalized rates, W_a/A and W_e/A, versus $kT/|\varepsilon|$ for various ε

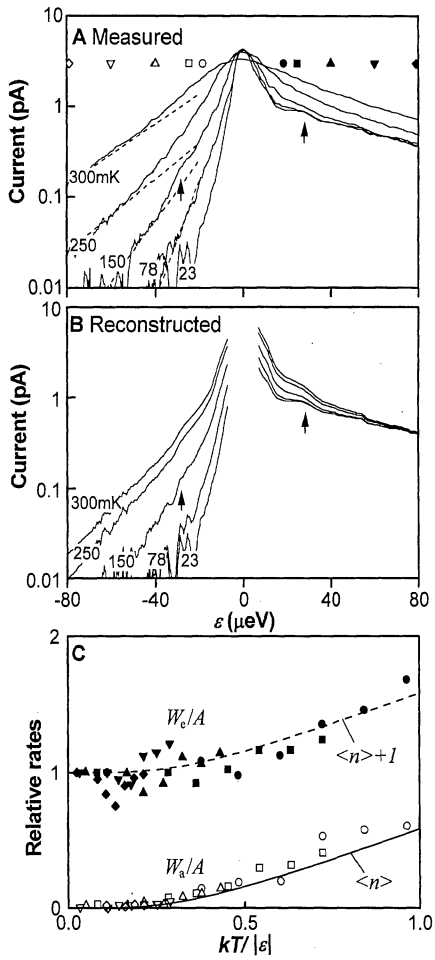

Fig. 2. (**A**) Measured current versus ε for $T = 23$ to 300 mK. The current is measured for eV_{SD} = 140 μeV while sweeping V_{GR} and V_{GL} simultaneously in opposite directions such that we change the energy difference ε. Gate voltage is translated to energy ε by a calibration better than 10% with photon-assisted tunneling measurements (*16*). Dashed lines indicate exponential dependence, $e^{\varepsilon/kT}$, for $|\varepsilon| \gg kT$. Arrows point at steplike structure on the emission side ($\varepsilon > 0$) and a shoulder on the absorption side ($\varepsilon < 0$). From fits (*11*) to the elastic current part at 23 mK, we obtained $h\Gamma_R \sim hT_c \sim 1$ μeV and $h\Gamma_L \sim 5$ μeV for this data set. (**B**) Reconstructed current, $I_{tot}(\varepsilon) = I_{el}(23\ \text{mK}) + I_{inel}(\varepsilon,T)$ for different T. The spontaneous emission spectra derived from the measured data at 23 mK and Eq. 1 are used to reconstruct the full temperature and energy dependence. (**C**) The absorption rate W_a (open symbols) and emission rate W_e (closed symbols) normalized by the spontaneous emission rate A versus $kT/|\varepsilon|$. Circles, squares, upper and lower triangles, and diamonds are taken at $|\varepsilon|$ = 18, 24, 40, 60, and 80 μeV, respectively [see also symbols in (A)]. The solid line indicates the Bose-Einstein distribution, $\langle n\rangle$, whereas the dashed line shows $\langle n\rangle + 1$.

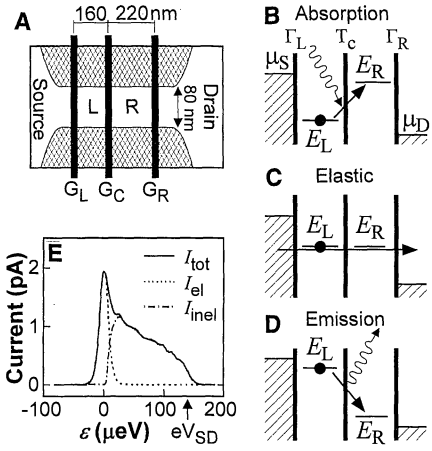

Fig. 1. (**A**) Double quantum dot device defined in the 2DEG of a AlGaAs-GaAs heterostructure by focused ion beam implantation. The narrow channel connects the large 2D source and drain leads. Negative voltages (V_{GL}, V_{GC}, and V_{GR}) applied to the metal gates (G_L, G_C, and G_R; widths are 40 nm) induce three tunable tunnel barriers in the wire. The two quantum dots, L and R, respectively, contain ~15 and ~25 electrons; charging energies are ~4 and ~1 meV; and the measured average spacing between single-particle states is ~0.5 and ~0.25 meV. (**B**, through **D**) Energy diagrams (vertical axis) along the spatial axis through the dots (horizontal axis) for the tunnel situations: absorption, elastic, and emission. Thick vertical lines denote tunnel barriers. The continuous electron states in the leads are filled up to the Fermi energies μ_S and μ_D. The external voltage V_{SD} between leads opens a transport window of size $eV_{SD} = \mu_S - \mu_D$. The energy, $\varepsilon \equiv E_L - E_R$, is defined as the difference between the topmost filled discrete state of the L dot, E_L, and the lowest discrete state for adding an extra electron to the R dot, E_R. (The interdot capacitance prevents that E_L and E_R are simultaneously occupied.) An elastic current can flow when $\varepsilon = 0$, otherwise a nonzero current requires absorption ($\varepsilon < 0$) or emission of energy ($\varepsilon > 0$). T_c is the tunnel coupling and Γ_i is the inelastic rate between the two dots. Γ_L and Γ_R are the tunnel rates across the left and the right barriers. (**E**) Typical measurement of the current (solid) versus ε at 23 mK. The measured current is decomposed in an elastic (dashed) and an inelastic (dotted-dashed) part.

and T up to 200 mK is shown in Fig. 2C. The measured data closely follow the prediction $[W_e - W_e]/A = 1$; that is, the normalized rates, W_a/A and W_e/A, differ by 1 over the temperature range $T < 200$ mK without fitting any parameter.

The inelastic rate for a two-level system coupled to a bosonic environment at $T = 0$ is expected to have a T_c^2 dependence (*14, 15*). Still, without identifying the bosonic environment, we can test this dependence on the elastic tunnel coupling T_c between the two dots. The inelastic current increases with T_c, as shown in Fig. 3A. For the largest coupling, we obtain a saturation where the elastic current peak can no longer be distinguished. By fitting the elastic current part to a Lorentzian line shape (*11*) we can obtain rough estimates for T_c as long as the current is less than the saturation value. We found that with these fitted values, the inelastic current scales as T_c^α with an exponent $\alpha = 2.5 \sim 3$, perhaps somewhat greater than expected. The effect of the increased coupling on the symmetric part of the current at low T is shown in Fig. 3B. For small tunnel coupling, we always obtain Lorentzian line shapes. For increasing couplings, the data still fit to a Lorentzian tail on the absorption side. However, we generally found significant deviations for small ε, implying that for large coupling the elastic and inelastic rates can become of the same order. This effect may form a significant limitation for the coherence time in coupled quantum devices (*16*).

The importance of fluctuations in the environment on electron tunneling through quantum devices has been recognized for a long time. Environmental studies on Coulomb blockade devices with two or more tunnel junctions have only discussed effects due to absorption (*3, 17*). For emission it is required that electrons are first pumped to a higher energy state, as has recently been done in a superconducting Cooper pair transistor under microwave irradiation (*18*). In the case of a double dot, pumping occurs when $E_L > E_R$ and an electron tunnels in from the left reservoir to E_L. A double dot thus offers a unique two-level system that is pumped by a dc voltage without the induction of heating currents. It is therefore possible to reach an out-of-equilibrium situation so close to $T = 0$ that vacuum fluctuations become the main source for generating electron transport.

To identify whether photons, plasmons, or phonons form the bosonic environment (*19*), we measured spontaneous emission spectra while placing the double dot in different electromagnetic environments. In the regime from 10 to 100 μeV, the typical wavelengths are 1 to 10 cm for photons and 0.3 to 30 cm for 2DEG plasmons. We tested the coupling to the photonic environment by placing the sample in microwave cavities of different size (*20*). To check the coupling to plasmons, we measured different types of devices with largely different dimensions of the 2DEG leads, gate pads, and bonding wires. Both types of variation had no effect on the emission spectra; even the fine structure was reproduced.

The third option of acoustic phonons is the most likely possibility (*21*). Phonon emission rates have been calculated for single dots (*22*). For a double dot system, we can obtain the general energy dependence (*15*). For a deformation potential, we expect a rate dependence of ε^{D-2} (ε for 3D phonons and constant for 2D phonons) and for piezoelectric interaction of ε^{D-4} ($1/\varepsilon$ for 3D phonons and $1/\varepsilon^2$ for 2D surface acoustic waves) (*23*). In Fig. 3C traces measured on two different types of devices are compared. Here, the emission current is plotted versus ε on a log-log scale. Ignoring the bumps, we found an energy dependence between $1/\varepsilon$ and $1/\varepsilon^2$. This result implies that the dominant emission mechanism is the piezoelectric interaction with 2D or 3D acoustic phonons. Note that a $1/\varepsilon$ or $1/\varepsilon^2$ dependence should be avoided in coherent devices, because the inelastic rate becomes large near resonance ($\varepsilon \sim 0$) (*16*).

The bumps observed in both type of devices suggest the existence of resonances, for instance, due to a finite size in the phonon environment. The bumps are particularly clear in the derivative of the current to energy (dotted curves in Fig. 3A). The large bump in Fig. 3A at $\varepsilon = 30$ μeV corresponds to a frequency of $f = \varepsilon/h = 7.3$ GHz. For 3D phonons, this yields a wavelength $\lambda^{3D} = s^{3D}/f = 640$ nm ($s^{3D} = 4800$ m/s is the 3D sound velocity), whereas for 2D surface acoustic waves $\lambda^{2D} = s^{2D}/f = 380$ nm ($s^{2D} = 2800$ m/s). Both wavelengths, more or less, fit with the dimensions of the two quantum dot devices. We have not yet been able to control these resonances by studying devices with a variety of gate dimensions. However, we predict that it will be possible to gain control over the phonon environment by making 3D phonon cavities in hanging bridges (*24*) or by creating a 2D phonon band gap with a periodic gate geometry (*25*).

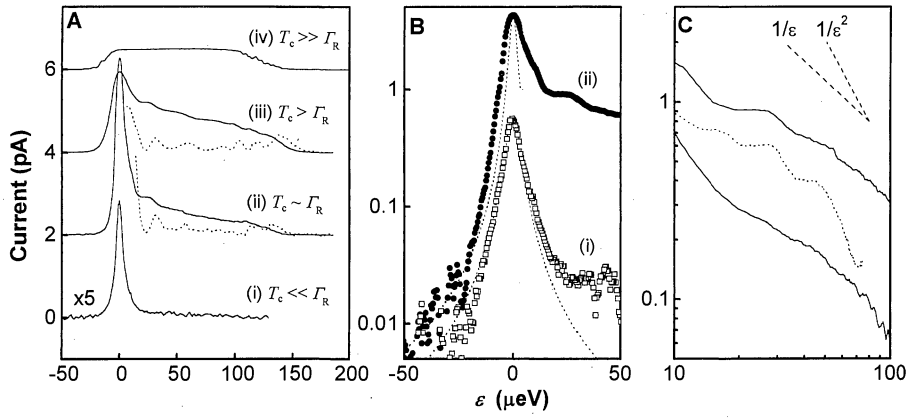

Fig. 3. Current spectrum for different coupling energies at 23 mK. (**A**) The magnetic field is 1.6 T for (i) and 2.4 T for the other curves (*10*). The curves have an offset, and curve (i) is multiplied by 5. Rough estimates for the coupling energies are (i) hT_c (~0.1 μeV; h is Planck's constant) $\ll h\Gamma_R$ (~10 μeV), (ii) $hT_c \approx h\Gamma_R$ (~1 μeV), (iii) $hT_c > h\Gamma_R$ (~0.1 μeV), and (iv) $hT_c \gg h\Gamma_R$ (~0.01 μeV), and $\Gamma_L \gtrsim \Gamma_R$ for all curves. The two dotted curves are the derivatives $-dI/d\varepsilon$ in arbitrary units for curves (i) and (ii) to enhance the bump structure. (**B**) Logarithmic-linear plots for (i) and (ii). Dashed lines are Lorentzian fits. For (ii) we chose parameters that fit the tail for negative ε. (**C**) Logarithmic-logarithmic plots of the emission spectrum for two different samples. The solid lines are based on the focused ion beam sample in Fig. 1A [upper trace is the same as (ii) in (A); lower trace is for coupling energies between (i) and (ii) in (A)]. The dotted line is based on a surface gate sample with a distance between left and right barriers of 600 nm (*12*). The dashed lines indicate a $1/\varepsilon$ and $1/\varepsilon^2$ dependence expected for piezoelectric interaction with 3D and 2D phonons, respectively.

References and Notes

1. H. Mizuta and T. Tanoue, *The Physics and Applications of Resonant Tunnelling Diodes* (Cambridge Univ. Press, Cambridge, 1995).
2. *The New Superconducting Electronics, Proceedings of a NATO Advanced Study Institute*, Waterville Valley, NH, 9 to 20 August 1992, H. Weinstock and R. W. Ralston, Eds. (Kluwer, Dordrecht, Netherlands, 1992), ser. E, vol. 251.
3. H. Grabert and M. H. Devoret, Eds., *Single Charge Tunneling* (Plenum, New York, 1992), ser. B, vol. 294.
4. P. L. McEuen, *Nature* **393**, 15 (1998); S. J. Tans, A. R. M. Verschueren, C. Dekker, *ibid.*, p. 49.
5. T. Fujisawa and S. Tarucha, *Superlattices Microstruct.* **21**, 247 (1997); *Jpn. J. Appl. Phys.* **36**, 4000 (1997).
6. For recent reviews, see R. Ashoori, *Nature* **379**, 413 (1996); L. P. Kouwenhoven and C. M. Marcus, *Phys. World* (June 1998), p. 35.
7. For a review, see L. P. Kouwenhoven *et al.*, in *Mesocopic Electron Transport, Proceedings of a NATO Advanced Study Institute*, Curaçao, Netherlands Antilles, 25 June to 5 July 1996, L. L. Sohn, L. P. Kouwenhoven, G. Schön, Eds. (Kluwer, Dordrecht, Netherlands, 1997), ser. E, vol. 345, pp. 105–214; available online at http://vortex.tn.tudelft.nl/~leok/papers/.
8. P. W. Milonni, *The Quantum Vacuum: An Introduction to Quantum Electrodynamics* (Academic Press, San Diego, CA, 1994).
9. The statistics of our inelastic emission should be regulated by the statistics of single-electron tunneling [A. Imamoglu and Y. Yamamoto, *Phys. Rev. B* **46**, 15982 (1992)].
10. The sample was cooled in a dilution refrigerator with a lowest temperature of 23 mK. Because of noise, the effective electron temperature is ~50 mK in the leads. In all measurements, we applied a perpendicular magnetic field between 1.6 and 2.4 T to maxi-

mize the single-particle spacing such that we could neglect transport through excited states.
11. The elastic current is given by the formula $I_{el}(\varepsilon) = eT_c^2\Gamma_R/[T_c^2(2 + \Gamma_R/\Gamma_L) + \Gamma_R^2/4 + (\varepsilon/h)^2]$; see Yu. V. Nazarov, *Phys. B* **189**, 57 (1993); T. H. Stoof and Yu. V. Nazarov, *Phys. Rev. B* **53**, 1050 (1996).
12. N. C. van der Vaart *et al.*, *Phys. Rev. Lett.* **74**, 4702 (1995).
13. Also, cotunneling can give excess current for $\varepsilon \neq 0$. In our measurements, however, the cotunneling current was less than 0.01 pA and can be neglected. For a review on cotunneling, see D. V. Averin and Yu. V. Nazarov, in (*3*), pp. 217–247.
14. A. J. Legget *et al.*, *Rev. Mod. Phys.* **59**, 1 (1987).
15. A T_c^2 dependence can also be obtained from perturbation theory when $T_c \ll \varepsilon$ [L. I. Glazman and K. A. Matveev, *Sov. Phys. JETP* **67**, 1276 (1988)].
16. We have reported a coherent coupling effect in double quantum dots using photon-assisted tunneling experiments [T. H. Oosterkamp *et al.*, *Nature*, in press]. These observations were made when a small bias voltage was applied. In this case, emission processes do not give rise to current.
17. Stimulated emission into the electromagnetic environment does play an important role for the presence of charging effects in single tunnel junctions [T. Holst *et al.*, *Phys. Rev. Lett.* **73**, 3455 (1994)].
18. Y. Nakamura, C. D. Chen, J. S. Tsai, *Phys. Rev. Lett.* **79**, 2328 (1997).
19. Bosonic excitations in a Fermi liquid (particle-hole excitations) can also be described as a bosonic bath with ohmic dissipation. For this case, the inelastic rate has a power-law dependence, $\Gamma(\varepsilon) \sim \varepsilon^{\gamma}$, where γ is related to the phase shift, δ, at the Fermi surface through $\gamma = 4/\pi^2\delta^2 - 1$ [see (*14*) and F. Guinea *et al.*, *Phys. Rev. B* **32**, 4410 (1985)]. Because $\delta^2 > 0$, the power $\gamma > -1$. This does not agree with our observed energy dependence, which is between $1/\varepsilon$ and $1/\varepsilon^2$.
20. We used a cylindrical cavity (diameter = 36 mm and height = 84 mm), which has a minimum resonance energy of about 20 μeV, and a rectangular cavity (22 mm by 19 mm by 8 mm) with resonance frequency of about 40 μeV.
21. Coupling to optical phonons is efficient only at much larger energies.
22. U. Bockelmann, *Phys. Rev. B* **50**, 17271 (1994).
23. For phonons, the inelastic rate at $T = 0$ can be written as $\Gamma_i \sim (T_c/\varepsilon)^2 J(\varepsilon)$, where $J(\varepsilon) \sim c^2(\varepsilon)g(\varepsilon)/\varepsilon$ is the spectral function and $c(\varepsilon)$ is the energy-dependent coupling (*14*). The phonon density of states $g(\varepsilon) \sim \varepsilon^{D-1}$ (D stands for dimension) such that $\Gamma_i \sim T_c^2 c^2(\varepsilon)\varepsilon^{D-4}$. When we neglect possible fine structure in $c(\varepsilon)$, we have for deformation $c \sim \varepsilon$ and thus $\Gamma_i \sim \varepsilon^{D-2}$, whereas for piezoelectric interaction c is constant and thus $\Gamma_i \sim \varepsilon^{D-4}$.
24. A. N. Cleland and M. L. Roukes, *Nature* **392**, 160 (1998).
25. J. M. Shilton *et al.*, *J. Phys. Condens. Matter* **8**, L531 (1997).
26. We thank M. Devoret, L. Glazman, S. Godijn, Y. Hirayama, J. Mooij, Yu. Nazarov, Y. Tohkura, N. Uesugi, M. Uilenreef, and N. van der Vaart for help and discussions. Supported by the Dutch Foundation for Fundamental Research on Matter (FOM) and L.P.K. by the Royal Netherlands Academy of Arts and Sciences.

28 July 1998; accepted 1 October 1998

Heterocyst Pattern Formation Controlled by a Diffusible Peptide

Ho-Sung Yoon and James W. Golden*

Many filamentous cyanobacteria grow as multicellular organisms that show a developmental pattern of single nitrogen-fixing heterocysts separated by approximately 10 vegetative cells. Overexpression of a 54–base-pair gene, *patS*, blocked heterocyst differentiation in *Anabaena* sp. strain PCC 7120. A *patS* null mutant showed an increased frequency of heterocysts and an abnormal pattern. Expression of a *patS-gfp* reporter was localized in developing proheterocysts. The addition of a synthetic peptide corresponding to the last five amino acids of PatS inhibited heterocyst development. PatS appears to control heterocyst pattern formation through intercellular signaling mechanisms.

The regulation of cell fate and pattern formation is a fundamental problem in developmental biology. Cell-cell communication often plays a key role in controlling development. Diffusible molecules that directly influence cell fate determination have been found in several eukaryotic organisms (*1*). Prokaryotic development in *Bacillus*, *Streptomyces*, and *Myxococcus* is also controlled by intercellular signaling (*2*, *3*). We have investigated the regulation of cell fate determination and pattern formation in a prokaryote that grows as a simple multicellular organism.

When the filamentous cyanobacterium *Anabaena* sp. strain PCC 7120 grows diazotrophically, approximately every tenth vegetative cell terminally differentiates into a heterocyst (*4*) (Fig. 1, A and B). This simple, one-dimensional developmental pattern spatially separates two incompatible processes: oxygen-evolving photosynthesis in vegetative cells and oxygen-sensitive nitrogen fixation in heterocysts. We have found that a small gene, *patS*, is crucial for the formation and maintenance of a normal heterocyst pattern.

The *patS* gene was identified on the conjugal cosmid 8E11 (*5*), which suppressed heterocyst development (Fig. 2A). A 3.3-kb subclone (pAM1035) was shown to confer the heterocyst-suppression phenotype (Het^s), and its sequence was determined (GenBank accession number AF046871). The same fragment isolated from an independent cosmid, 13C12, produced the same phenotype, indicating that the dominant Het^s phenotype is a property of wild-type sequences. An analysis of subcloned fragments in shuttle vectors (Fig. 2A) prompted us to investigate a small, 51–base pair (bp), open reading frame (ORF) named *patS* (Fig. 2B).

A 140-bp polymerase chain reaction (PCR) fragment containing the *patS* ORF (pAM1686) conferred the Het^s phenotype (Fig. 2A). Overexpression of *patS* by the *Anabaena* PCC 7120 *glnA* promoter (pAM1691) completely blocked heterocyst formation (Figs. 1C and 2A). The antisense orientation (pAM1695) produced no noticeable phenotype. *patS* blocks development at an early stage because even the cryptic pattern of nonfluorescent cells, which is produced by some developmental mutants (*6*), was not observed.

To test whether different levels of transcription correlate with the degree of heterocyst inhibition, we placed *patS* under the control of the copper-inducible *petE* promoter (P_{petE}) (*7*) (Fig. 3A). Without the addition of $CuSO_4$, the strain containing P_{petE}-*patS* was wild type. As *patS* transcription was increased by the addition of $CuSO_4$, there was a corresponding decrease in the frequency of heterocysts. We observed no influence of $CuSO_4$ on heterocyst development when *patS* was cloned in the reverse orientation (Fig. 3A).

Mutations in *patS* resulted in a loss of the ability to suppress heterocysts. pAM1882 (Fig. 2A) was mutagenized and screened for plasmids that failed to suppress heterocysts (*8*). Four plasmids were identified, each with a missense mutation within *patS* (Fig. 2B).

patS potentially encodes a 17–amino acid peptide, starting at the first available ATG codon; however, other in-frame ATG and GTG codons are present. PatS has no homologs or sequence motifs in the databases. It contains a stretch of five hydrophobic amino acids in its NH_2-terminal half, and its COOH-terminal half is mostly hydrophilic.

A *patS-lacZ* translational fusion showed that *patS* is translated and developmentally regulated (*9*). β-galactosidase (β-Gal)–specific activity of the in-frame fusion (Fig. 2C) increased about threefold (to 6000 units) during the 6 hours after the heterocyst induction and then decreased to the preinduction level after 27 hours. A direct analysis of the *patS* message on RNA blots yielded similar results

Department of Biology, Texas A&M University, College Station, TX 77843–3258, USA.

*To whom correspondence should be addressed.